Enhanced broadband absorption in gold by plasmonic tapered coaxial holes

Lei Mo,[1,2] Liu Yang,[1,3,*] Achim Nadzeyka,[4] Sven Bauerdick,[4] and Sailing He[1,5]

[1] *Centre for Optical and Electromagnetic Research, State Key Laboratory of Modern Optical Instrumentation, Zhejiang University, Hangzhou 310058, China*
[2]*Department of Physics, Zhejiang University, Hangzhou 310027, China*
[3]*School of Electrical, Computer, and Energy Engineering, Arizona State University, Tempe, Arizona 85287, USA*
[4]*Raith GmbH, Konrad-Adenauer-Allee 8, 44263 Dortmund, Germany*
[5]*Department of Electromagnetic Engineering, JORCEP, School of Electrical Engineering, Royal Institute of Technology (KTH), S-100 44 Stockholm, Sweden*

[*]*optyang@zju.edu.cn*

Abstract: Gold absorbers based on plasmonic tapered coaxial holes (PTCHs) are demonstrated theoretically and experimentally. An average absorption of over 0.93 is obtained theoretically in a broad wavelength range from 300 nm to 900 nm without polarization sensitivity due to the structural symmetry. Strong scattering of the incident light by the tapered coaxial holes is the main reason for the high absorption in the short wavelength range below about 550 nm, while gap surface plasmon polaritons propagating along the taper dominate the resonance-induced high absorption in the long wavelength range. Combining two PTCHs with different structural parameters can further enhance the absorption and thus increase the spectral bandwidth, which is verified by a sample fabricated by focused ion beam milling. This design is promising to be extended to other metals to realize effective and efficient light harvesting and absorption.

OCIS codes: (160.3918) Metamaterials, (240.6680) Surface plasmons, (300.1030) Absorption.

References and links

1. C. M. Watts, X. L. Liu and W. J. Padilla, "Metamaterial electromagnetic wave absorbers," Adv. Mater. **24**(23): OP98–OP120 (2012).
2. Y. X. Cui, Y. R. He, Y. Jin, F. Ding, L. Yang, Y. Q. Ye, S. M. Zhong, Y. Y. Lin and S. He, "Plasmonic and metamaterial structures as electromagnetic absorbers," Laser Photon. Rev. **8**(4): 495-520 (2014).
3. H. A. Atwater and A. Polman, "Plasmonics for improved photovoltaic devices," Nat. Mater. **9**(3): 205-213 (2010).
4. A. Lenert, D. M. Bierman, Y. Nam, W. R. Chan, I. Celanovic, M. Soljacic and E. N. Wang, "A nanophotonic solar thermophotovoltaic device," Nat. Nanotechnol. **9**(2):126-130 (2014).
5. V. Rinnerbauer, A. Lenert, D. M. Bierman, Y. X. Yeng, W. R. Chan, R. D. Geil, J. J. Senkevich, J. D. Joannopoulos, E. N. Wang, M. Soljačić and I. Celanovic, "Metallic photonic crystal absorber-emitter for efficient spectral control in high-temperature solar thermophotovoltaics," Adv. Energy. Mater. **4**(12): 1400334 (2014).
6. D. Kraemer, B. Poudel, H. P. Feng, J. C. Caylor, B. Yu, X. Yan, Y. Ma, X. W. Wang, D. Z. Wang and A. Muto, "High-performance flat-panel solar thermoelectric generators with high thermal concentration," Nat. Mater. **10**(7): 532-538 (2011).
7. J. B. Pendry, "Controlling light on the nanoscale," Progress In Electromagnetics Research **147**: 117-126 (2014).
8. N. I. Landy, S. Sajuyigbe, J. J. Mock, D. R. Smith, W. J. Padilla, "Perfect metamaterial absorber," Phys. Rev. Lett. **100**: 207402 (2008).
9. J. M. Hao, J. Wang, X. L. Liu, W. J. Padilla, L. Zhou and M. Qiu, "High performance optical absorber based on a plasmonic metamaterial," Appl. Phys. Lett. **96**(25): 251104 (2010).
10. A. Moreau, C. Ciraci, J. J. Mock, R. T. Hill, Q. Wang, B. J. Wiley, A. Chikoti and D. R. Smith, "Controlled-reflectance surfaces with film-coupled colloidal nanoantennas," Nature **492**(7427): 86-89 (2012).
11. M. G. Nielsen, A. Pors, O. Albrektsen and S. I. Bozhevolnyi, "Efficient absorption of visible radiation by gap plasmon resonators," Opt. Express **20**(12):13311-13319 (2012).

#224829 - $15.00 USD Received 29 Oct 2014; revised 10 Dec 2014; accepted 11 Dec 2014; published 22 Dec 2014

12. K. Aydin, V. E. Ferry, R. M. Briggs and H. A. Atwater, "Broadband polarization-independent resonant light absorption using ultrathin plasmonic super absorbers," Nat. Commun. **2**:517 (2011).
13. Y. X. Cui, J. Xu, K. H. Fung, Y. Jin, S. He, N. X. Fang, "A thin film broadband absorber basedon multi-sized nanoantennas," Appl. Phys. Lett. **99**(25): 253101 (2011).
14. M. K. Hedayati, M. Javaherirahim, B. Mozooni, R. Abdelaziz, A. Tavassolizadeh, V. S. K. Chakravadhanula, V. Zaporojtchenko, T. Strunkus, F. Faupel and M. Elbahri, "Design of a perfect black absorber at visible frequencies using plasmonic metamaterials," Adv. Mater. **23**(45): 5410-5414 (2011).
15. Y. Q. Ye, Y. Jin, and S. He, "Omnidirectional, polarization-insensitive and broadband thin absorber in the terahertz regime,"J. Opt. Soc. Am. B **27**(3): 498-504 (2010).
16. Y. X. Cui, K. H. Fung, J. Xu, H. J. Ma, Y. Jin, S. He and N. X. Fang, "Ultrabroadband light absorption by a sawtooth anisotropic metamaterial slab," Nano Lett. **12**(3): 1443-1447 (2012).
17. F. Ding, Y. X. Cui, X. C. Ge, Y. Jin and S. He, "Ultra-broadband microwave metamaterial absorber," Appl. Phys. Lett. **100**(10): 103506 (2012).
18. J. A. Schuller, E. S. Barnard, W. S. Cai, Y. C. Jun, J. S. White and M. L. Brongersma, "Plasmonics for extreme light concentration and manipulation," Nat. Mater. **9**(3): 193-204 (2010).
19. T. Søndergaard, S. M. Novikov, T. Holmgaard, R. L. Eriksen, J. Beermann, Z. H. Han, K. Pedersen and S. I. Bozhevolnyi, "Plasmonic black gold by adiabatic nanofocusing and absorption of light in ultra-sharp convex grooves," Nat. Commun. **3**: 969 (2012).
20. F. Zhang, L. Yang, Y. Jin, and S. He, "Turn a highly-reflective metal into an omnidirectional broadband absorber by coating a purely-dielectric thin layer of grating," Progress In Electromagnetics Research **134**: 95-109 (2013).
21. F. I. Baida, A. Belkhir, D. V. Labeke and O. Lamrous, "Subwavelength metallic coaxial waveguides in the optical range: Role of the plasmonic modes," Phys. Rev. B **74**(20): 205419 (2006).
22. W. J. Fan, S. Zhang, B. Minhas, K. J. Malloy, S. R. J. Brueck, "Enhanced infrared transmission through subwavelength coaxial metallic arrays," Phys. Rev. Lett. **94**(3): 033902 (2005).
23. R. D. Waele, S. P. Burgos, A. Polman and H. A. Atwater, "Plasmon dispersion in coaxial waveguides from single-cavity optical transmission measurements," Nano Lett. **9**(8): 2832-2837 (2009).
24. S. P. Burgos, R. D. Waele, A. Polman and H. A. Atwater, "A single-layer wide-angle negative-index metamaterial at visible frequencies," Nat. Mater. **9**(5): 407-412 (2010).
25. J. F. Zhang, J. Y. Ou, N. Papasimakis, Y. F. Chen, K. F. Macdonald and N. I. Zheludev, "Continuous metal plasmonic frequency selective surfaces," Opt. Express **19**(23): 23279-23285 (2011).
26. A. A. E. Saleh and J. A. Dionne, "Toward efficient optical trapping of sub-10-nm particles with coaxial plasmonic apertures," Nano Lett. **12**(11): 5581-5586 (2012).
27. S. I. Bozhevolnyi, V. S. Volkov, E. Devaux, J. Y. Laluet and T. W. Ebbesen, "Channel plasmon subwavelength waveguide components including interferometers and ring resonators," Nature **440**(7083): 508-511 (2006).
28. P. B. Johnson and R. W. Christy, "Optical constants of noble metals," Phys. Rev. B **6**(12): 4370-4379 (1972).

1. Introduction

Perfect electromagnetic wave absorbers, which absorb all incident electromagnetic waves without any reflection or transmission, are very important devices or elements for many applications [1, 2], e.g. imaging, sensing, emitting, etc. Particularly in the visible and near-infrared wavelength range covering the solar spectrum, broadband absorbers become critically important for sunlight harvesting and conversion [3-6]. In addition to the direct conversion of sunlight into electricity through semiconductors, another efficient way to utilize the solar energy is to generate heat through some high-loss metals or nanomaterials (e.g. carbon nanotubes [4]). The heat can be accumulated to heat water, or be further converted into electricity through thermophotovoltaics [4, 5] or thermoelectric materials [6]. Most metals, e.g. gold (Au), silver, aluminium, etc. are good reflectors in the visible and near-infrared wavelength range and are difficult to be made absorptive in such a broad wavelength range.

As the development of nanophotonics and nanofabrications, various metallic metamaterials are proposed to realize perfect absorbers, where both electric and magnetic resonances can be excited simultaneously, and 100% absorption is achievable [7, 8]. Three-layer configurations of a dielectric layer sandwiched between two nanostructured metallic layers are widely adopted [8-10]. However, their absorption spectra are always limited due to the resonant properties [8-10]. Fortunately, the spectrum can be expanded when different resonators of different resonating frequencies are mixed together, e.g., by distributing different resonators in one period [11-14] or stacking multiple metal-dielectric layers [15-17]. Particularly in the stacked multi-layer configuration, a more expanded absorption spectrum

#224829 - $15.00 USD Received 29 Oct 2014; revised 10 Dec 2014; accepted 11 Dec 2014; published 22 Dec 2014

can be obtained due to non-resonant slowlight modes induced by multiple resonances [16, 17]. In the solar spectral range, resonances in the metamaterial absorbers are always modified by surface plasmon polaritons (SPPs) due to the dielectric properties of the compositional metals [2, 18]. It is well-known that SPPs have a strong ability to route and manipulate photons in a subwavelength region [2, 18], where photons can be strongly absorbed by the compositional metallic and/or lossy dielectric materials [3, 11-17]. More than one material is contained in all these absorbers, making fabrication more complex [3, 11-17]. Søndergaard et al. proposed a one-material non-resonant broadband absorber based on Au ultra-sharp convex grooves via adiabatic nanofocusing of gap SPPs [19]. Fabrication processes are simplified, requiring only focused ion beam (FIB) milling. However, the milling parameters should be controlled very carefully and kept stable over time to achieve the ultra-fine nanogrooves. In our previous work, the highly-reflective Au was made to be black by simply coating a thin, purely dielectric layer of a slot waveguide grating, where multiple optical mechanisms/effects could be excited simultaneously [20]. As mentioned before, two different materials were involved, making the fabrication a little more difficult.

In this work, we demonstrate an effective broadband absorber based on metallic coaxial holes, which are always straight and have been widely investigated, e.g., for waveguiding [21], enhanced optical transmission [22, 23], negative-index metamaterials [24], color selection [25], nanoparticle manipulation [26], etc. However, it is very difficult to obtain a broadband absorber by directly employing those straight coaxial holes [21-26]. Here, less sharp tapers are proposed to be introduced into both the outer sidewalls of the holes and the inner pillars. Such structures become plasmonic tapered coaxial holes (PTCHs), consisting of only one metallic material and being able to be fabricated by FIB milling. Even though it is expensive and sometimes time-consuming, FIB milling is still one of the most straightforward and accurate tools to make nanostructures into metals [19, 21-26]. It is also very easy to fabricate tapers into metals [27]. Both simulation and experimental results show that two-different-sized PTCHs alternatively distributed in each period are able to greatly enhance the absorption in the near-infrared wavelength range, turning the highly reflective metal black.

2. Structure and simulation method

Our absorber is schematically shown in Fig. 1, which consists of a periodic array of Au PTCHs with tapered inner pillars and outer sidewalls of holes. Full-field simulations were performed with a finite-difference time domain (FDTD) method by Lumerical FDTD Solutions. As shown in Fig. 1(c), a plane wave with its wavelength (λ) ranging from 300 nm to 1300 nm is considered as the light source incident from the top at an angle of θ and an azimuth angle of φ for both *s*- and *p*-polarizations. For normal incidence, only *s*-polarized wave is considered because of the polarization-independent optical properties determined by the symmetric structure. Bloch boundaries were set along the x and y directions, while perfectly matched layers were treated in the z direction. The dielectric constants of Au are obtained by fitting the data from [28]. Reflection (R) is monitored to obtain the absorption (A) by $A = 1 - R$, because the Au film milled with PTCHs is thick enough to allow little light transmission.

In Fig. 1(b), all the structural parameters are illustrated. The period, P, always affects the operation wavelength band of a device. For Au, we set $P = 400$ nm in this paper to enable our absorber to operate in the solar spectral range. The hole depth, H, is usually a parameter affecting the resonances supported in a vertical hole [20-23]. A 400-nm deep hole in Au is deep enough to support many resonances once the light is coupled into it. Therefore, $H = 400$ nm is considered. For a fixed H, d_t and d_b determine the gradient of the inner pillar, while D_t and D_b determine the gradient of the outer sidewall of the hole. All of them, in order to determine the taper of the coaxial hole, need to be optimized carefully before fabrication. To characterize the whole absorption properties with one value, an average absorption, A_{ave}, in the wavelength range of 300-900 nm is defined, which covers the main solar spectrum and takes up about 66.3% of all the solar energy. A high A_{ave} means high absorption in the range of

#224829 - $15.00 USD Received 29 Oct 2014; revised 10 Dec 2014; accepted 11 Dec 2014; published 22 Dec 2014

300 nm ≤ λ ≤ 900 nm. In the following, optimal d_t, d_b, D_t and D_b are to be obtained to have the highest A_{ave} under normal illumination of the light (until otherwise specified).

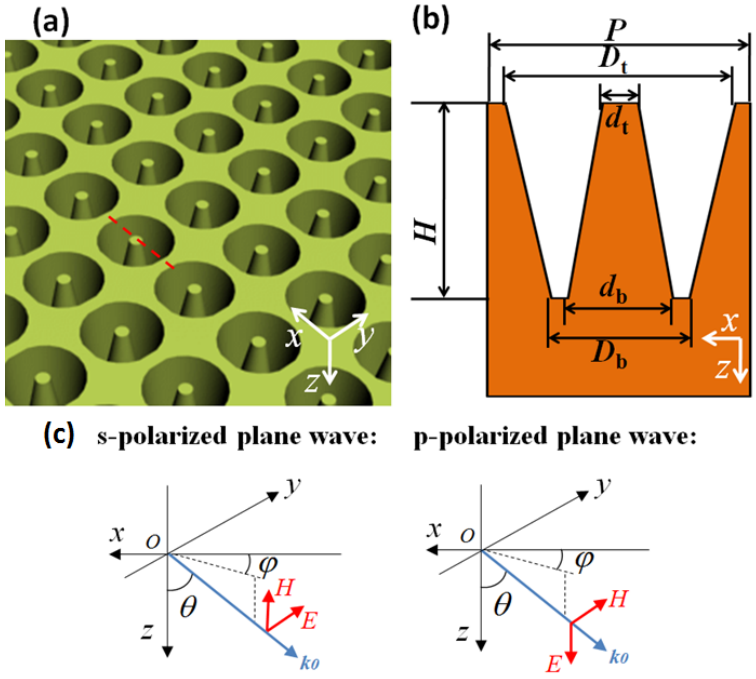

Fig. 1. (a) Three-dimensional schematic diagram of PTCH-based absorber. (b) Cross section of one unit cell in the *xz* plane along the red dashed line in (a) with all the structural parameters illustrated. (c) *s*- and *p*-polarized plane waves are considered as the light source incident from the top.

3. Optical analysis

3.1 Absorbers based on a single-sized PTCH

First, the outer sidewall of the hole is fixed with D_t = 350 nm and D_b = 250 nm. A_{ave} as a function of both d_t and d_b is calculated and shown in Fig. 2(a), where the cases of $d_t > d_b$ are not considered due to the structure not very easy to fabricate and moreover the possible weak coupling of light. From this figure, one can see that when the bottom of the pillar touches the bottom of the hole, i.e. $d_b = D_b$ = 250 nm, and the top diameter is d_t = 80 nm, A_{ave} becomes as high as 0.854. For each d_t, A_{ave} reaches its maximum just when $d_b = D_b$ holds. Next, we fix $d_b = D_b$ and set d_t = 80 nm to optimize D_t and D_b. Fig. 2(b) shows that much higher A_{ave} of approximately 0.916 can be achieved at D_t = 410 nm and D_b from 270 nm to 310 nm, which is indicated by a black dotted line segment. Point "A" (marked by a black cross) in this segment at $D_b = d_b$ = 270 nm and D_t = 410 nm is chosen as a start of a second optimization cycle. Fig. 2(c) shows that a very small enhancement of only 0.003 (i.e. A_{ave} = 0.919) is obtained after a second optimization when d_t moves from the original optimal value of 80 nm to 70 nm, which are well within the fabrication tolerance. Then d_t = 70 nm and $d_b = D_b$ are set to optimize D_b and D_t again in terms of A_{ave}, which is shown in Fig. 2(d). It is seen that the maximal A_{ave} of approximately 0.919 maintains and still exists at the line of D_t = 410 nm and D_b from 270 nm to 310 nm, indicated by the black dotted line segment in Fig. 2(d). The insignificant enhancement of A_{ave} clearly suggests that the first optimization cycle is sufficiently accurate to obtain an optimal structure with high enough A_{ave}. It is also seen that changing d_t and D_b does

#224829 - $15.00 USD Received 29 Oct 2014; revised 10 Dec 2014; accepted 11 Dec 2014; published 22 Dec 2014

not affect the A_{ave} very much, as shown in Figs. 2(b)-2(d), which means the strong tolerance of our design to the top diameter of the inner pillar, d_t, and the bottom diameters of the outer hole or the inner pillar, $D_b = d_b$.

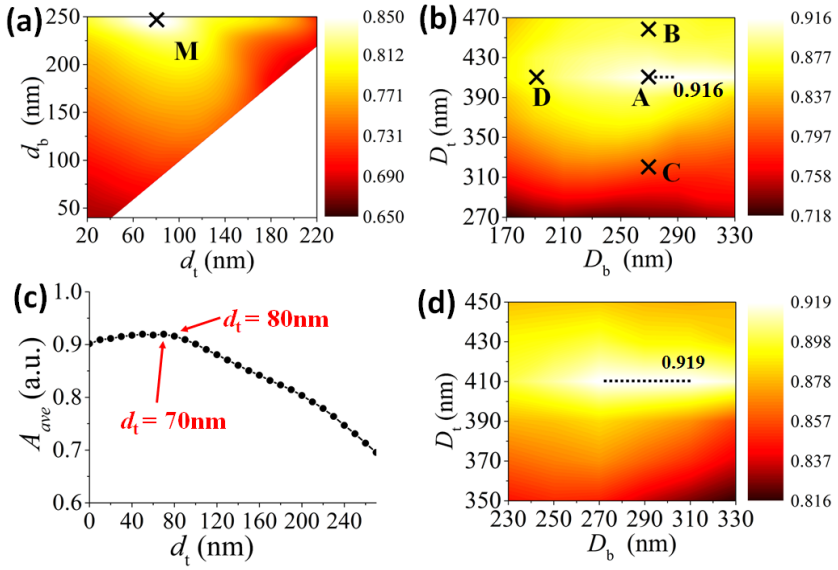

Fig. 2. The average integrated absorption, A_{ave}, as a function of (a) the top and bottom diameters of the inner pillar, i.e. d_t and d_b with D_t = 350 nm and D_b = 250 nm; and (b) the top and bottom diameter of the outer hole, i.e. D_t and D_b with $D_b = d_b$ and d_t = 80 nm. Maximal A_{ave} = 0.854 is achieved at $d_b = D_b$ and d_t = 80 nm and marked as "M" by the black cross in (a). In (b), maximal A_{ave} of approximately 0.916 is achieved and indicated by the black dotted line segment with D_t = 410 nm and D_b from 270 nm to 310 nm. Point "A" in this segment at $D_b = d_b$ = 270 nm and D_t = 410 nm is marked by the black cross. Three black cross markers: "B" at D_b = 270 nm and D_t = 460 nm, "C" at D_b = 270 nm and D_t = 320 nm, "D" at D_b = 200 nm and D_t = 410 nm, are illustrated for comparison. A second optimization cycle of (c) d_t with $D_b = d_b$ = 270 nm and D_t = 410 nm; (d) D_t and D_b with $D_b = d_b$ and d_t = 70 nm in terms of A_{ave}. In (d), maximal A_{ave} of approximately 0.919 is achieved and indicated by the black dotted line segment with D_t = 410 nm and D_b from 270 nm to 310 nm.

Since the average absorption is very sensitive to D_t as shown in Figs. 2(b) and 2(d), we choose and compare the absorption spectra at three typical points in Fig. 2(b), e.g. Points "A", "B", and "C" at D_t = 410, 460 and 320 nm respectively, to help us understand the light absorption mechanism within the PTCHs. They have the same $D_b = d_b$ = 270 nm and d_t = 80 nm. Their absorption spectra are shown in Fig. 3(a). For the optimal absorber based on PTCH A, it is seen from Fig. 3(a) that the absorption of Au can be greatly enhanced by the PTCHs in the short wavelength range below about 550 nm where Au is intrinsically highly absorptive. Light incident on the top coaxial hole arrays is strongly scattered into the holes, being absorbed there. Beyond this short wavelength range, the absorption is still very high until the wavelength increases to about 900 nm, even though Au is highly reflective in this range. In comparison, the absorption spectrum of the PTCH B based absorber blue shifts and has fewer absorption peaks. This is mainly due to the larger opening and the slower tapering of the coaxial holes for PTCH B, forming a weakly-trapping cavity for the photons in the long wavelength range beyond about 700 nm. Therefore, its A_{ave} (= 0.869) is lower. For the absorber based on PTCH C, reduced absorption in the short wavelength range below about 550 nm can be observed due to the difficulty for light to enter into the coaxial holes of much smaller openings, while apparent ripples appear in the long wavelength range (especially around 850 nm, where there is a very deep absorption valley) due to the steeper sidewalls of

#224829 - $15.00 USD Received 29 Oct 2014; revised 10 Dec 2014; accepted 11 Dec 2014; published 22 Dec 2014

the outer holes forming a stronger resonating cavity. Therefore, it has a much lower A_{ave} (= 0.789) than the absorbers based on PTCHs A and B.

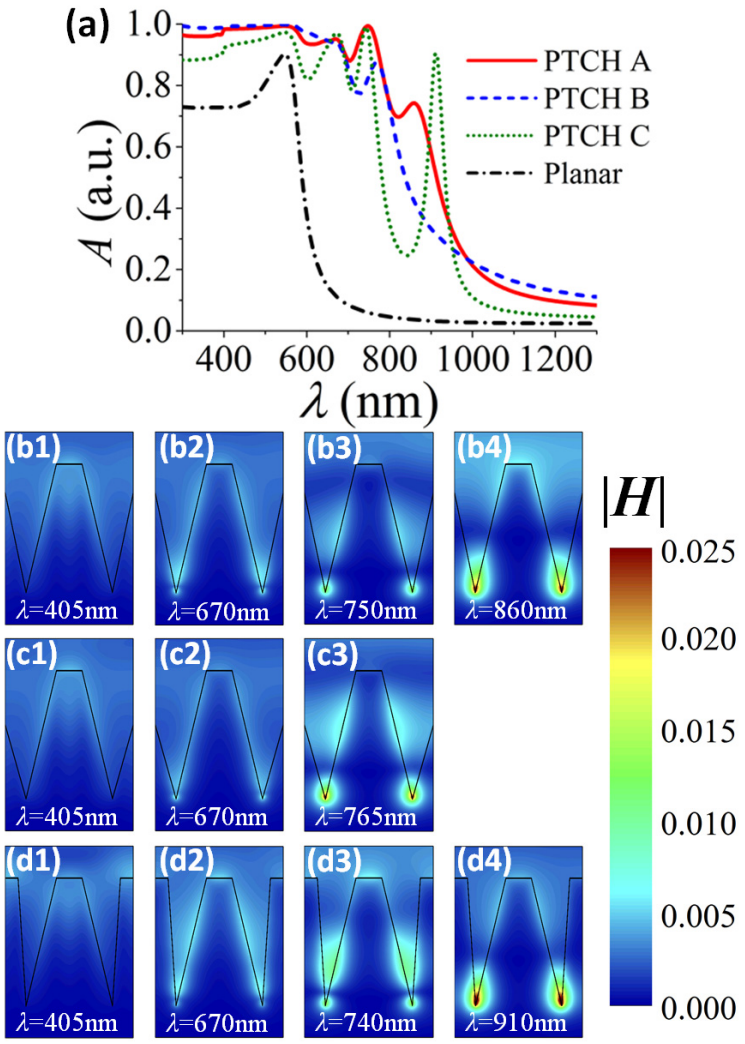

Fig. 3. (a) Absorption spectra of the absorbers based on PTCH A (red solid curve) and PTCH B (blue dashed curve) and PTCH C (green dotted curve), as well as the planar Au film (the black dash-dotted curve) for comparison. (b-d) Magnetic field distributions, $|H|$, in the xz plane at typical wavelengths for absorbers based on PTCH A: (b1) λ = 405 nm, (b2) 670 nm, (b3) 750 nm, and (b4) 860 nm; PTCH B: (c1) λ = 405 nm, (c2) 670 nm, and (c3) 765 nm; and PTCH C: (c1) λ = 405 nm, (c2) 670 nm, (c3) 740 nm, and (c4) 910 nm.

More details about the light trapping behaviors in the PTCHs are illustrated in Figs. 3(b)-3(d)) in terms of the magnetic field distributions, $|H|$, of the three absorbers at their peak wavelengths as well as at λ = 405 nm, where an asymmetric increase of the absorption appears for both absorbers based on PTCHs A and C in Fig. 3(a). At λ = 405 nm, SPPs are excited propagating along the top surface of the holes, which can be seen in Figs. 3(b1), 3(c1) and 3(d1), with their effective wavelengths of approximately 405 nm for all the three absorbers. For the PTCH B based absorber with a large D_t = 460 nm, short-wavelength photons can be easily scattered into the holes and absorbed there, leading to a quite high absorption close to 1

#224829 - $15.00 USD Received 29 Oct 2014; revised 10 Dec 2014; accepted 11 Dec 2014; published 22 Dec 2014

in this wavelength range and thus a very slight absorption increase at λ = 405 nm observed in Fig. 3(a). In the long wavelength range beyond about 550 nm, light can be coupled into the gaps, becoming gap SPPs, and the gap SPPs resonate between the top and bottom of the PTCHs. As shown in Figs. 3(b2-b4), the 3rd, 2nd, 1st resonances are excited in the gap of the coaxial hole for the optimal absorber based PTCH A at λ = 670, 750, and 860 nm, respectively. Meanwhile, as the gap becomes increasingly narrow, the effective refractive index of the gap SPPs increases. When approaching the bottom, the propagating gap SPPs will gradually slow down and be localized around the taper tip. As the wavelength increases, such localization becomes even stronger. For example, at λ = 860 nm of the PTCH A based absorber shown in Fig. 3(b4), the magnetic field is much more strongly confined at the taper tip than at λ = 670 and 750 nm as shown in Figs. 3(b2-b3). The absorbers based on PTCHs B and C behaves similarly. For the PTCH C based absorber with a smaller D_t of 410 nm, the gap becomes a stronger cavity, resulting in stronger resonances and localization within it. Hence, the 1st resonance red shifts to λ = 910 nm as shown in Fig. 3(d4), in comparison with that for the optimal absorber shown in Fig. 3(b4). In contrast, for PTCH B based absorber with a larger D_t of 460 nm, only 3rd and 2nd resonances are excited with the magnetic field of the 2nd one loosely confined in the gap as shown in Figs. 3(c2-c3). Therefore, its absorption spectrum bandwidth is limited.

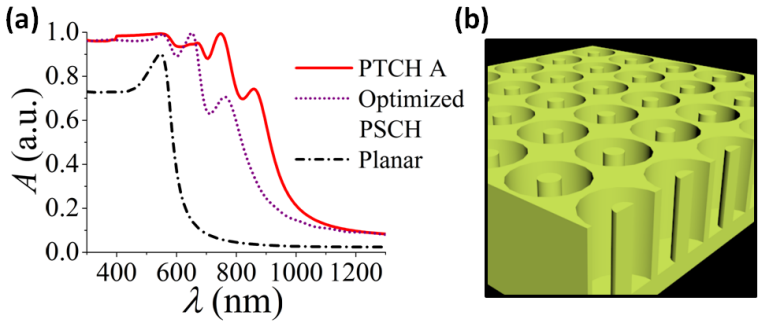

Fig. 4. (a) Absorption spectra of the absorbers based on PTCH A (red solid curve) and the optimized PSCH (pink dotted curve), as well as the planar Au film (black dash-dotted curve) for comparison. (b) Three-dimensional schematic diagram of PSCHs.

In Fig. 4(a), the absorption spectrum of an optimized plasmonic straight coaxial holes (PSCHs; schematically shown in Fig. 4(b)) is also plotted and compared with that of the optimal absorber based on PTCH A. The optimal structural parameters of the PSCH obtained by the same above simulation method are P = 240 nm, $d_t = d_b$ = 80 nm and $D_t = D_b$ = 230 nm with H = 400 nm kept the same as that of PTCH A. It is seen from Fig. 4(a) that the absorption of the PSCHs drops in the wavelength range from about 650 nm to 1100 nm compared with that of PTCH A, leading to a much smaller value of A_{ave}, i.e. A_{ave} = 0.845 (versus A_{ave} = 0.916 for PTCH A). This result illustrates that broadband absorbers cannot be achieved even with optimal PSCHs, whose absorption spectrum fortunately can be greatly improved and extended by simply introducing tapers to both the inner pillar and the outer hole, i.e. our PTCHs. This confirms again the important role of the localized gap SPPs in the tapered coaxial holes (which is quite different from those reported in [21-26]) on the enhanced absorption in the long wavelength range as shown in Fig. 4(a).

For our absorber based on PTCH A, we also investigated the absorption spectra at different incident and azimuth angles for both *s*- and *p*-polarizations. Some typical spectra are shown in Fig. 5. For *s*-polarization, the absorption spectra keep almost unchanged until the incident angle, θ, becomes larger than 30° for various azimuth angles, namely, φ = 0°, 30° and 45°. The absorption spectrum starts to drop at θ = 45° and drops quickly when θ becomes larger for all the considered azimuth angles (especially for the largest φ, i.e. φ = 45°), as shown in Figs. 4(a), 4(c) and 4(e). Fortunately, for *p*-polarization, the absorption spectrum in

#224829 - $15.00 USD Received 29 Oct 2014; revised 10 Dec 2014; accepted 11 Dec 2014; published 22 Dec 2014

the long wavelength range beyond about 550 nm increases as θ increases to 60° (where the absorption spectrum becomes irregular and apparently not as good as the spectra when $\theta \leq$ 45°), while in the short wavelength range below about 550 nm does not change much when θ ranges from 0 to 60°, for all the azimuth angles considered here as shown in Figs. 4(b), 4(d) and 4(f). Therefore, our PTCH based absorber can perform very well (even better for *p*-polarization) in a large incident angle range.

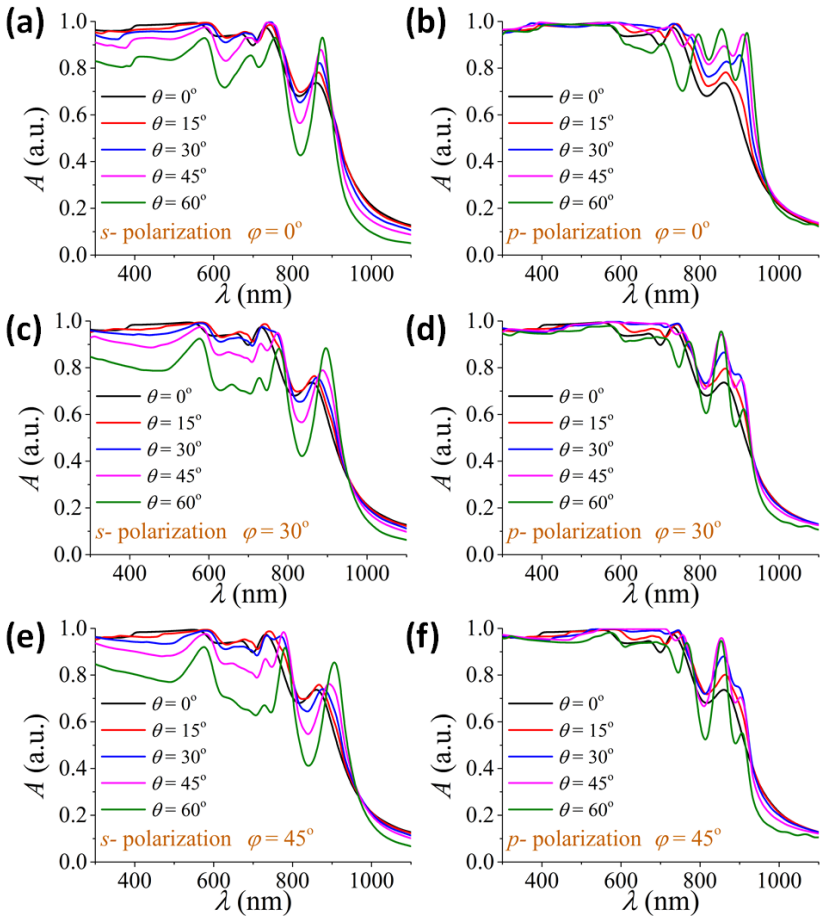

Fig. 5. Absorption spectra at various typical incident (θ) and azimuth (φ) angles for both *s*- and *p*-polarizations for PTCH A.

3.2 Absorbers based on Combined PTCHs

In Fig. 2(b), there is always a maximal A_{ave} at D_t = 410 nm for each D_b. Here, we select Point "D" at D_t = 410 nm and D_b = 200 nm in Fig. 2(b) as one PTCH to be combined with PTCH A. The A_{ave} at this point is only 0.887, lower than that at Point "A". It has very similar spectral characteristics with that of the absorber based on PTCH A except the narrower bandwidth shown in Fig. 6(a), which is induced by the blue shift of the resonances as shown in Figs. 6(c1-c3). Much higher absorption is also achieved in a relatively broad wavelength range by the PTCH D based absorber than the planar one shown in Fig. 6(a).

Interestingly, the absorption of the absorber based on PTCH A in the wavelength range of 800-900 nm can be greatly enhanced when combining PTCHs A and D alternatively, as schematically shown in Fig. 6(b), even though the absorption spectrum of the absorber based

#224829 - $15.00 USD Received 29 Oct 2014; revised 10 Dec 2014; accepted 11 Dec 2014; published 22 Dec 2014

on PTCH D starts to drop quickly in this range, as shown in Fig. 6(a). A_{ave} (= 0.9345) of this combined absorber becomes much higher than that of each composite (A_{ave} = 0.916 and 0.887 for the absorbers based on PTCHs A and D, respectively). The two strong resonant absorption peaks at λ = 830 and 880 nm are the main contributors. Their corresponding magnetic field distributions are shown in Figs. 6(d2-d3). It is very interesting that at λ = 880 nm (830 nm), where the original absorption of the PTCH A (PTCH D) based absorber is much higher than that of the PTCH D (PTCH A) based absorber, the magnetic field distribution is mainly confined in the gaps of PTCH A (PTCH D) after combination. In comparison, at λ = 730 nm, where the original absorptions for both composite absorbers are almost equal as shown in Fig. 6(a), the magnetic field is approximately evenly distributed in the combined PTCHs as shown in Fig. 6(d1).

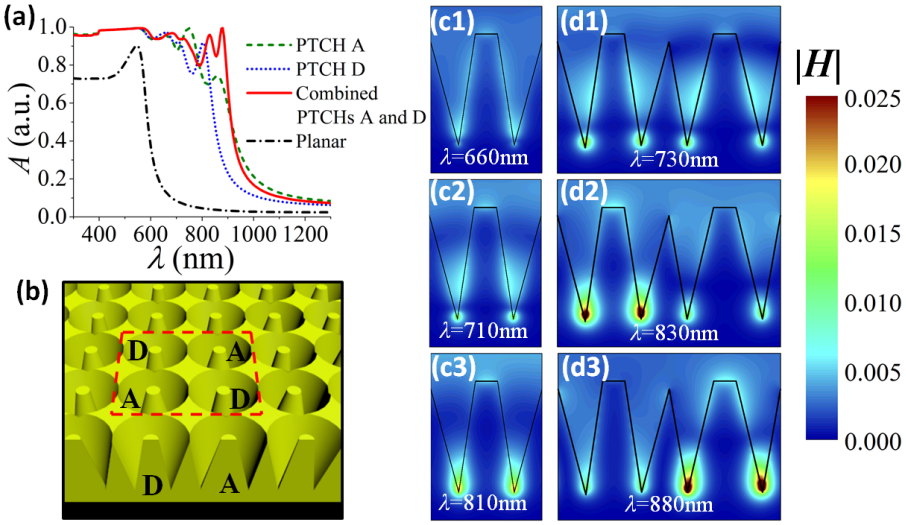

Fig. 6. (a) Absorption spectra of different PTCH arrays based on: PTCH A (green dashed curve), PTCH D (blue dotted curve), and the combined structure of PTCHs A and D (red solid curve), as well as of a planar Au film (black dash-dotted curve) for comparison. (b) Three-dimensional schematic diagram of the combined absorber structure based on PTCHs A and D. Magnetic field distributions, $|H|$, in the xz plane at peak wavelengths for PTCH D: (c1) λ = 660 nm, (c2) 710 nm, and (c3) 810 nm; and the combined PTCHs: (d1) λ = 730 nm, (d2) 830 nm, and (d3) 880 nm.

4. Experimental results

According to the design of the combined absorber based on PTCHs A and D, we fabricated it by FIB milling (Raith ionLiNE; acceleration voltage of 35 kV and beam current of 2.7 pA) in a 500 nm thick Au film deposited on a silicon substrate by sputtering. Its scanning electron microscope (SEM) image is shown in Fig. 7(a), with zoomed-in images shown in Fig. 7(b) and 7(c). It can be seen that the PTCHs are well fabricated with good repeatability over a relatively large area, about 20.8 × 20.8 μm^2, including 52 × 52 PTCHs in total. However, the structural parameters are a little bit different from the designed values due to fabrication errors. Through careful inspection of the SEM images in Fig. 7, the average structural parameters are determined, i.e. $d_t \approx 130$ nm, $D_t \approx 420$ nm, $d_b = D_b \approx 230$ nm for PTCH A and $d_t \approx 100$ nm, $D_t \approx 450$ nm, $d_b = D_b \approx 160$ nm for PTCH D. The depth is about 40 nm deeper than the designed structure, i.e. $H \approx 440$ nm.

#224829 - $15.00 USD Received 29 Oct 2014; revised 10 Dec 2014; accepted 11 Dec 2014; published 22 Dec 2014

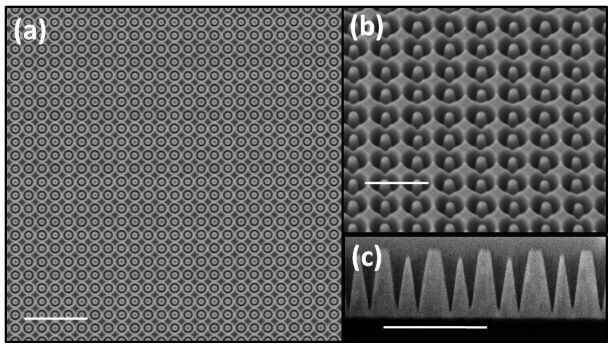

Fig. 7. SEM images of the combined absorber based on PTCHs A and B milled in Au: (a) top-view (scale bar: 2 μm); (b) tilted-view (scale bar: 800 nm); and (c) cross-section (scale bar: 800 nm).

A home-built microspectroscopy (schematically shown in Fig. 8) is employed to measure the reflection properties of the sample. Because of the symmetric structure, a non-polarized light source is used here. First, a broadband light source (NKT Photonics, SuperK COMPACT) is focused onto the PTCH area through a 10× objective (N. A. = 0.25). The reflected light is collected by the same objective and split into two beams by a 50:50 beam splitter. One is introduced to a CCD (charge coupled device) in order to observe and align the sample under the input light illumination. The other passes through a square aperture with side length of 100 μm, which is inserted to eliminate the stray light and guarantee that the received light by the spectrometer is merely from the central sample area (about 10 × 10 μm^2 in this work). For the measurement in the short wavelength range of below 900 nm, a spectrometer (Ocean Optics, USB2000) is employed directly and controlled by a computer to do the wavelength scanning. Below 400 nm, the received signal is excluded due to the high noise. In the long wavelength range of 900-1300 nm, a monochrometer (Zolix, Omni-λ1509) is used in conjunction with an InGaAs detector, also working in a remote operation mode. The directly measured reflection spectra are calibrated carefully with three perfect mirrors with reflection of over 99.5% in the wavelength ranges of 400-700 nm, 700-900 nm and 0.9-10 μm, respectively.

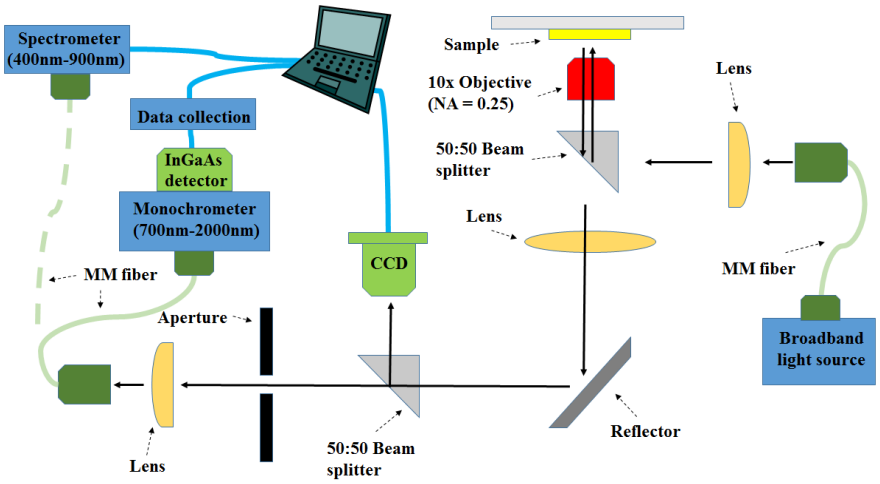

Fig. 8. Schematic diagram of our home-built microspectroscopy to measure the reflection spectra of our samples. The green dashed curve means that the multimode (MM) fiber receiving the focused light from the aperture can be switched to connect either the spectrometer or the monochrometer.

#224829 - $15.00 USD Received 29 Oct 2014; revised 10 Dec 2014; accepted 11 Dec 2014; published 22 Dec 2014

Fig. 9 shows the measured reflection spectrum of the combined absorber based on PTCHs A and D, which is much lower over a much broader wavelength range than that of a planar Au film with the same thickness. This is verified to be an effective way to make the highly reflective Au to be black. However, for the planar absorber, its reflection blue shifts about 100 nm from the corresponding simulated curve based on the designed structural parameters, which is probably due to the different dispersive fitting curves of Au used in simulation [27] from the real material properties, the deviation between the measurement set-up and the simulation conditions, etc. For our combined absorber, the two reflection peaks in the wavelength range of 700-900 nm match well with those in the simulation, but the two short-wavelength peaks behave similarly to the planar absorber and blue shift to the shorter wavelengths. Such a mismatch between the measurement and the simulation based on the designed structural parameters might also be attributed to the small geometrical discrepancy between the fabricated and simulated PTCHs, the non-uniformity of the fabricated sample, gallium doping into the Au during milling (causing changes of the material's dispersive property), etc. in addition to the possible reasons for the blue shift of the reflection spectrum of the planar absorber.

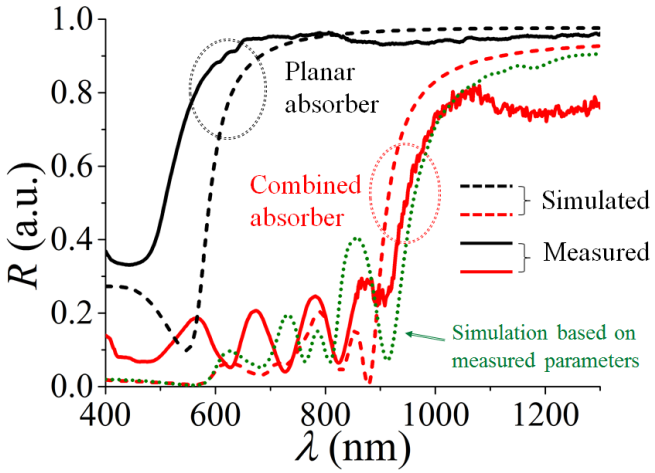

Fig. 9. Measured (solid curves) and simulated (dashed curves) reflection spectra for the combined absorber (red curves) and a planar Au thin film with the same thickness (black curves), respectively. The simulation is based on the designed structural parameters. For comparison, the simulated reflection spectrum based on the SEM-inspected structural parameters is also plotted and indicated by a green dotted curve. The measured structural parameters are $d_t \approx 130$ nm, $D_t \approx 420$ nm, $d_b = D_b \approx 230$ nm for PTCH A and $d_t \approx 100$ nm, $D_t \approx 450$ nm, $d_b = D_b \approx 160$ nm for PTCH D as well as $H \approx 440$ nm.

In order to find the main reason behind the strong resonances appearing in the measured reflection spectrum as shown in Fig. 9, we performed an additional simulation based on the SEM-inspected structural parameters as mentioned above and plotted the simulated reflection spectrum (indicated by the green dotted curve) in the same figure for comparison. Like the experimental result, the newly simulated spectrum based on the experimental values shows stronger resonances with four apparent reflection peaks than the simulated result based on the designed values. Two of the peaks in the long wavelength range match well with those of the measured spectrum. Meanwhile, the steep quickly-rising trend of the spectrum is also very close to the experimental one. Such good match verifies the simulation method very well. However, the fairly large mismatch between the simulation results based on the measured and designed values indicates that the fabrication errors are the main contributors for the quite different spectrum obtained experimentally. The other two reflection peaks in the short wavelength range red shift to longer wavelengths in comparison with the experimental

#224829 - $15.00 USD Received 29 Oct 2014; revised 10 Dec 2014; accepted 11 Dec 2014; published 22 Dec 2014

spectrum. This behavior is not only similar to the simulated spectrum based on the designed values (even though the equivalent reflection peaks are very small) , but also to the simulated spectrum of the planar Au thin film absorber. As a result, it can be confirmed that the dispersive fitting curves of Au used in the simulations [27] are different from the real material properties (which can also be changed by gallium doping during FIB milling), especially in the short wavelength range below about 700 nm. Meanwhile, the simple ideal simulation settings, e.g. the plane wave source, the normal incidence, etc. (which are very difficult to realize in a real measurement set-up) are also likely to cause the spectral shift between the measurement and the simulation results.

5. Conclusion

In summary, a PTCH-based broadband absorber was investigated theoretically and experimentally. A very high absorption with A_{ave} = 0.9345 was achieved theoretically in a very broad wavelength range from 300 nm to 900 nm. The absorber is also polarization-independent due to the structural symmetry. Our experimental results verify the numerical design and the trapping mechanisms within it. It is also shown that FIB milling is a versatile and reliable technique for easy fabrication of complex 3D structures. We believe that our universal design can be extended to other metals to realize effective and efficient light harvesting and absorption.

Acknowledgments

This work was partially supported by the National Natural Science Foundation of China (Nos. 61307078, 91233208, and 91233119), the National High Technology Research and Development Program (863) of China (No. 2012AA030402), the Zhejiang Provincial Key Project (No. 2011C11024), the Specialized Research Fund for the Doctoral Program of Higher Education (No. 20130101120134) and the Fundamental Research Funds for the Central Universities. L. Yang also acknowledges financial support from China Scholarship Council.